PNAS

Main Manuscript for

Temperature dependence of parasitoid infection and abundance of a diatom revealed by automated imaging and classification

Dylan Catlett[1], Emily E Peacock[1], E Taylor Crockford[1], Joe Futrelle[1], Sidney Batchelder[1], Bethany L F Stevens[1], Rebecca J Gast[1], Weifeng G Zhang[1], Heidi M Sosik[1]

[1]Woods Hole Oceanographic Institution

*Correspondence: Dylan Catlett

Email: dylan.catlett@whoi.edu

Author Contributions: DC, EEP, HMS designed the study; EEP, ETC, BLFS, RJG, WGZ, HMS contributed sample and data collection; DC, EEP, ETC, JF, SB, BLFS, RJG, WGZ, HMS contributed to data management and analysis; DC, HMS wrote the manuscript; all authors contributed to and edited the manuscript and approved for submission

Competing Interest Statement: The authors declare no competing interests.

Classification: Biology; Environmental Sciences

Keywords: diatom, protistan parasite, Imaging FlowCytobot, machine learning, Guinardia delicatula

This PDF file includes:

Main Text
Figures 1 to 6

Abstract

Diatoms are a group of phytoplankton that contribute disproportionately to global primary production. Traditional paradigms that suggest diatoms are consumed primarily by larger zooplankton are challenged by sporadic parasitic “epidemics” within diatom populations, but our understanding of diatom parasitism is limited by difficulties in quantifying these interactions. Here, we observe the dynamics of *Cryothecomonas aestivalis* (a protist) infection of an important diatom on the Northeast U.S. Shelf (NES), *Guinardia delicatula*, with a combination of automated imaging-in-flow cytometry and a convolutional neural network image classifier. Application of the classifier to >1 billion images from a nearshore time series and >20 survey cruises across the broader NES reveals the spatiotemporal gradients and temperature dependence of *G. delicatula* abundance and infection dynamics. Suppression of parasitoid infection at temperatures <4 °C drives annual cycles in both *G. delicatula* infection and abundance, with an annual maximum in infection observed in the fall-winter preceding an annual maximum in host abundance in the winter-spring. This annual cycle likely varies spatially across the NES in response to variable

annual cycles in water temperature. We show that infection remains suppressed for ~2 months following cold periods, possibly due to temperature-induced local extinctions of the *C. aestivalis* strain(s) that infect *G. delicatula*. These findings have implications for predicting impacts of a warming NES surface ocean on *G. delicatula* abundance and infection dynamics and demonstrate the potential of automated plankton imaging and classification to quantify phytoplankton parasitism in nature across unprecedented spatiotemporal scales.

Significance Statement

Diatoms are unicellular algae whose “blooms” are associated with high primary productivity, prolific fisheries, and carbon flux to the deep ocean. Despite its potential impact on marine food webs, diatom parasitism is poorly understood due to challenges observing its prevalence and environmental controls at appropriate spatiotemporal scales. Here we use automated plankton imaging and machine learning classification to elucidate abundance and parasitic infection dynamics of a biomass-dominant diatom on the Northeast U.S. Shelf. We suggest that temperature indirectly regulates diatom abundance via direct suppression of parasitism. This temperature dependence implies that ongoing warming may enable parasitic infection to occur throughout the year, driving dramatic shifts in this diatom’s abundance dynamics with potential cascading effects on the Northeast U.S. Shelf ecosystem.

Main Text

Introduction

Diatoms are a major source of oceanic primary production and play an outsized role in marine ecosystems and global biogeochemistry (1, 2). Diatoms frequently accumulate in response to nutrient enrichment of the surface ocean, and these “blooms” likely result in productive marine food webs and fisheries (1, 3). Traditional oceanographic paradigms explain this association by arguing that diatom production is predominantly consumed by large micro- and meso-zooplankton which provide an efficient link to higher trophic levels (3–5). Diatoms can also be infected by smaller eukaryotic parasites and parasitoids (parasites that kill their hosts) as demonstrated by sporadic observations of “epidemics” within some diatom populations over the past several decades (6–8). While amplicon sequencing surveys have revealed a high diversity of putative eukaryotic parasites and many potential interactions with diverse diatoms (9, 10), the time, cost, and technical expertise required to make direct observations of diatom parasitism have thus far limited understanding of its prevalence, spatiotemporal dynamics, and oceanographic forcings (8).

One known example of diatom parasitism involves infection of the diatom, *Guinardia delicatula*, by the Cercozoan nanoflagellate, *Cryothecomonas aestivalis* (11). In this system the parasitoid penetrates the host's cell wall and subsequently consumes the host protoplast from within, resulting in host mortality. After consuming its host, the enlarged *C. aestivalis* cell divides several (usually 3, occasionally more) times within the frustule to create swarmers that reenter the free-living plankton community, often leaving fecal pellets behind in the host frustule (11). *C. aestivalis* is known to infect *G. delicatula* in the North and Wadden Seas (7). More recently, a study at the nearshore Martha's Vineyard Coastal Observatory (MVCO) found recurrent, widespread infection of *G. delicatula* by *C. aestivalis* in a 7-year time series of manually-annotated plankton images collected by Imaging FlowCytobot (IFCB) (12). In that study, infection by *C. aestivalis* was often found to regulate the magnitude of *G. delicatula* accumulation. When temperatures fell below 4 °C, however, infection was suppressed and accumulation of the host was frequently observed (12). This study combined with recent advances in automated image classification (13–15) demonstrate a path to develop automated, high-throughput approaches to quantify diatom parasitism on unprecedented spatiotemporal scales, and in turn fill a major gap in our knowledge of the prevalence, ecological significance, and oceanographic determinants of infection.

Here, we develop and apply an automated, machine learning-based classifier to >1 billion IFCB images gathered from >300,000 samples from the Northeast U.S. Shelf (NES) to quantify *G. delicatula* abundance and infection by *C. aestivalis*. The classifier is trained, optimized, and validated with a large set of manually annotated *G. delicatula* images including uninfected and infected chains. We apply the classifier to quantify *G. delicatula* abundance and infection prevalence with daily resolution across an in situ, ~15-year time series at MVCO and with ~10 km resolution across a spatial domain extending from the northern Gulf of Maine to the southern Mid-Atlantic Bight sampled during 23 cruises conducted across 9 years. Our results support a previous study's findings of recurrent, significant levels of infection of *G. delicatula* and a suppression of infection at temperatures <4 °C at the nearshore MVCO. Use of the automated classifier enabled discovery of continued suppression of infection for at least 60 days following these cold temperatures and observations of comparable infection dynamics across a spatial domain spanning from Cape Hatteras to Nova Scotia. Integrating genetic observations with the imaging results suggested high niche diversity within the *C. aestivalis* species complex and that cold temperatures result in local extinction of the strain parasitizing *G. delicatula*. A long-term reduction in the spatiotemporal extent of waters with temperature <4 °C indicates continued warming on the NES may reshape *G. delicatula* abundance and infection dynamics. In addition to elucidating the large-scale biogeography of *C. aestivalis* infection of *G. delicatula* on the NES, this study demonstrates the potential for automated plankton imaging coupled with artificial intelligence to advance knowledge of the understudied dynamics of phytoplankton-parasite interactions.

Results

Spatiotemporal dynamics of G. delicatula *abundance and infection on the Northeast U.S. Shelf*

G. delicatula was observed at relatively high abundances (>5 chains ml^{-1}) throughout the NES and was often found at extremely high abundance (>50 chains ml^{-1}) at the nearshore MVCO time series site (Fig. 1). A cross-shore gradient in *G. delicatula* abundances was evident across most of the NES, with high abundances close to shore declining to near-zero abundances beyond the shelf break (Fig. 1A). Low abundances were also observed in deep waters of the Gulf of Maine. *G. delicatula* abundances were highest in the northern Mid-Atlantic Bight and on Georges Bank, with relatively high abundances also seen on the Scotian Shelf. *G. delicatula* infection prevalence (Fig. 1B) was low (<5%) across most of the NES, but the spatial distribution showed a similar pattern to that of total *G. delicatula* abundance on the northern Mid-Atlantic Bight and Georges Bank. Areas associated with relatively high infection in these regions generally mirrored those associated with high abundance. Notably, infection was limited in nearshore waters of the Scotian

Shelf despite relatively high *G. delicatula* abundances. Low *G. delicatula* abundance in offshore waters of the NES and in most of the Gulf of Maine drove high uncertainty in infection prevalence. Mean sea surface temperatures (SST) (Fig. 1C) across the NES were typically >20 °C offshore of the shelf break and in the southern portion of the Mid-Atlantic Bight, 15-20 °C in the northern Mid-Atlantic Bight, and 10 °C or colder in the northern Gulf of Maine and Scotian Shelf. Infection prevalence appeared to be lowest in the cooler northern Gulf of Maine and Scotian Shelf, while high aggregate *G. delicatula* abundances were found across a broad range of mean temperatures except >20 °C.

Daily IFCB time series of *G. delicatula* abundance and infection prevalence alongside daily mean water temperature at MVCO provide a detailed view of temporal dynamics at a nearshore site on the NES, with intermittent amplicon sequencing observations providing additional insight into the dynamics of the parasitoid at this site (Fig. 1D-E). *G. delicatula* abundance and infection prevalence were often higher at MVCO than across the broader NES, regularly reaching abundances >50 chains ml^{-1} and infection prevalence >20%. High abundances were most often observed in the winter during or immediately following periods where water temperature was <4 °C and infection prevalence was negligible, in agreement with previous observations (12). *G. delicatula* also accumulated at other times of year when temperatures were warmer, but during these events abundances rarely exceeded 50 chains ml^{-1}. Parasitoid infection was most prevalent in the fall, with infection prevalence values of 20% or higher regularly observed prior to the seasonal onset of temperatures <4 °C. Infection prevalence was typically low during the spring and early summer, even when *G. delicatula* reached moderately high abundances and temperature exceeded 4 °C. Interestingly, at least some of the five *C. aestivalis* amplicon sequence variants (ASVs, a genetic proxy for strains or species) were detected at MVCO throughout the year, including during periods cooler than 4 °C and in the spring and summer when *G. delicatula* infection prevalence was negligible.

Observations show seasonal variations in the distributions of *G. delicatula* abundance and infection prevalence and in SST across the NES (Fig. 2). While only one cruise with limited coverage of the Gulf of Maine, Scotian Shelf, and southern Mid-Atlantic Bight was conducted during the winter, *G. delicatula* abundances were elevated (>20 chains ml^{-1}) and infection prevalence was high compared to other seasons across much of the NES. Mean winter-time SSTs on the NES were generally <10 °C and were <4 °C in many nearshore locations. *G. delicatula* abundance remained high across much of the Mid-Atlantic Bight and Georges Bank during the spring, with a notable nearshore band of elevated abundance also observed in the Gulf of Maine. Where infection prevalence was measurable during the spring, it was generally lower than in winter despite mean SSTs ≥~10 °C. *G. delicatula* abundances were low (<5 chains ml^{-1}) across much of the NES during the summer and infection prevalence was generally not quantifiable when seasonal mean SST was highest across most of the domain. The exception was at the northern edge of the domain including the Scotian Shelf and a small portion of the northern Gulf of Maine where high *G. delicatula* abundances coincided with negligible infection and relatively cool SSTs. In the fall, *G. delicatula* was typically not detected throughout the Gulf of Maine and Scotian Shelf, while intermediate abundances (~5 chains ml^{-1}) and SSTs associated with relatively high (>5%) infection prevalence were observed in several locations across the Mid-Atlantic Bight and Georges Bank.

Spatial and temporal gradients in G. delicatula *abundance and infection*

Distinct annual cycles were observed in *G. delicatula* abundance and infection prevalence both at MVCO and across the broader NES (Fig. 3A-B). Monthly aggregate *G. delicatula* abundances were highest in the winter and spring while infection prevalence was highest during the fall. From October to December at MVCO, aggregate *G. delicatula* abundance was approximately 5 chains ml^{-1} or less coinciding with high aggregate infection prevalence of ~10-12%. Monthly aggregate abundances increased to ~10 chains ml^{-1} in January until reaching an annual maximum of >30

chains ml^{-1} in March. This increase in monthly aggregate abundance coincided with a decline in aggregate infection prevalence to ~4% in January and an annual minimum of <1% in March. Comparable patterns were observed across the broader NES, although monthly aggregate abundance and infection prevalence values were lower and more uncertain due to less intensive sampling and lower host abundances.

A pronounced cross-shore decline in *G. delicatula* abundance was observed across the NES (Fig. 3C), with aggregate abundances of ~7 chains ml^{-1} within 50 km of the coastline declining to 2.30 chains ml^{-1} between 50-100 km from the coast and <2 chains ml^{-1} beyond 100 km from the coast. Consistent cross-shore gradients in infection prevalence were not observed, although values were generally higher offshore. Across the four NES Ecological Production Units (16, 17), relatively high aggregate *G. delicatula* abundances (>2.5 chains ml^{-1}) were observed in the Mid-Atlantic Bight and on Georges Bank and the Scotian Shelf, with lower aggregate abundances (<1.5 chains ml^{-1}) found in the Gulf of Maine. Aggregate infection prevalence ranged from 0.7-1.3% in the Mid-Atlantic Bight, Georges Bank, and Gulf of Maine regions had similar but was reduced (<0.5%) on the Scotian Shelf.

Role of temperature in governing G. delicatula *infection*

Previous observations (12) and our results suggest that water temperatures <4 °C provide *G. delicatula* with a refuge from parasitoid infection. The more extensive results we report here confirm the critical role of temperature in governing parasitoid infection of *G. delicatula* at MVCO (Fig. 4A) and across the broader NES (Fig. 4B). At MVCO, high *G. delicatula* abundance coincident with low infection prevalence (typically <2%) was observed frequently at temperatures <4 °C as observed previously via manual image classification (12). High *G. delicatula* abundances were also regularly observed when temperatures exceeded 4 °C but were often associated with non-negligible (>5%), and at times high (>20%), infection prevalence. Observations across the broader NES made possible by the automated classifier supported this pattern, with negligible infection prevalence found in all samples collected in waters colder than 4 °C except one (associated with high uncertainty). A small number (22 of 4219) of daily observations at MVCO had non-negligible infection prevalence (>5%) coincident with *G. delicatula* abundances >3 chains ml^{-1} at temperatures <4 °C. Most (18 of 22) of these daily observations were due to erroneous automated image classification, while the others were a result of high-resolution sampling and uncertainty in temperature observations (Supporting Text).

A bootstrap-aggregated ensemble of 100 regression tree models fit to predict infection prevalence from temperature showed the largest change in infection prevalence partial dependence at temperature thresholds of 4.6 and 4.1 °C in the MVCO and shipboard data, respectively (Fig. 4C). In both data sets infection prevalence partial dependence increased substantially at these thresholds. At MVCO, the partial dependence of infection prevalence was elevated at temperature values ranging from 4.6-17.6 °C, and showed a sharp decline when temperatures were >17.6 °C. However, the number of daily observations of elevated *G. delicatula* abundance was also lower around this upper threshold relative to the 4.6 °C threshold. In shipboard observations, the partial dependence of infection declined and remained low at temperatures >7.5 °C.

The high-resolution time series and well-resolved annual cycles in *G. delicatula* abundance and infection enabled by the automated classifier (Figs. 2-4) suggest that parasitoid infection of *G. delicatula* continues to be suppressed for some time after temperatures have warmed above 4 °C in spring. We investigated this further by computing the frequency of days at MVCO with *G. delicatula* abundance >5 chains ml^{-1} coinciding with and without infection prevalence >5% as a function of the number of days since the last observation of mean daily temperature <4 °C in each year (which we refer to hereafter as the end of the “cold snap”; Fig. 5). Across 14 years at MVCO with adequate data availability (see Fig. 1D-E), *G. delicatula* was found at high abundance

frequently (>300 total days) within 60 days of the end of the cold snap, but <2% of these days coincided with infection prevalence >5% (Fig. 5A). High *G. delicatula* abundances were found in conjunction with high infection prevalence within 30 days of the cold snap only in 2012 when the preceding cold snap lasted only 3 days. Observations of infection events were also rare within 60 days of the end of the cold snap, only occurring in 2012 and 2013 and accounting for a cumulative total of 6 of the 88 days where high *G. delicatula* abundances were observed (Fig. 5B). Variable patterns of detection of the five *C. aestivalis* ASVs at MVCO, including frequent detection of two ASVs during and following the cold snap, suggest that some strains of *C. aestivalis* survive the cold snap (Fig. 5C). Interestingly, however, the most abundant *C. aestivalis* ASV at MVCO was only detected from June-December (Fig. 5C) and was never detected during or within 70 days of the termination of the cold snap.

Long-term trend in the duration and areal extent of cold snaps on the NES

A long-term warming trend of 0.37 °C decade^{-1} was recently reported on the NES (18). Our results suggest this warming trend could have significant impacts on the dynamics of *G. delicatula* abundance and infection by *C. aestivalis* if it contributes to a decline in the duration and areal extent of cold snaps. More detailed analysis of the satellite SST record from 1982-2022 showed that the areal extent of cold snaps on the NES follows a clear seasonal cycle with the maximum areal extent observed during the winter as expected (Fig. 6A). However, over this time period the spatiotemporal extent of cold snaps has declined at an average rate of -2.1 x 10^4 d km yr^{-1}, indicating a likely reduction in the extent of *G. delicatula*'s thermal refuge from parasitism in this region (Fig. 6B). Extreme realizations of short-lived and spatially restricted cold snaps were also more frequent in the final decade of the 40-year satellite record, with the 5 shortest and/or spatially restricted cold snaps observed in 2012, 2016, 2020, 2021, and 2022 (Fig. 6B).

Discussion

Summary

We used automated, in situ imaging and a convolutional neural network image classifier to quantify, characterize the spatiotemporal distributions and gradients in, and determine the role of temperature in controlling *G. delicatula* abundance and parasitoid infection on the NES. We found that *G. delicatula* reached high abundance (>20 chains ml^{-1}) throughout the NES. The highest *G. delicatula* abundances were observed in the winter and spring in the nearshore Mid-Atlantic Bight and on Georges Bank, with high abundances also found during the summer on the Scotian Shelf. Parasitoid infection of *G. delicatula* was most prevalent in the fall in the Mid-Atlantic Bight and on Georges Bank but became negligible when temperatures fell below 4 °C. Here we discuss the physical and biological controls on *G. delicatula* abundance and infection dynamics and their implications with respect to ongoing warming of the NES surface ocean. We conclude with a discussion of the current limitations and future potential for automated imaging and machine learning classification to advance understanding of phytoplankton-parasite interactions.

Gradients in and controls on G. delicatula *abundance and infection dynamics on the NES*

Since *G. delicatula* is one of the biomass-dominant diatoms on the NES (12), understanding its abundance dynamics and the fates of its production under variable oceanographic conditions is an important step in predicting the response of the NES ecosystem to anthropogenic climate forcing. Our results revealed two prominent gradients in *G. delicatula* abundances. First, a prominent cross-shore gradient was found, with the highest abundances consistently observed close to shore (Figs. 1-3). This gradient in *G. deliatula* abundances follows the cross-shelf decline in phytoplankton and diatom biomass previously observed across the NES (19–22). These gradients are typically attributed to increased nutrient loading in the nearshore NES due to terrestrial and estuarine inputs (21, 22), which likely contributes to the cross-shore gradient in *G.*

delicatula abundances observed here. Conversely, cross-shore gradients in *G. delicatula* infection prevalence were not resolved here due to high uncertainty in offshore estimates. Nonetheless, persistently higher aggregate *G. delicatula* abundances and infection prevalence found at the near-shore MVCO relative to the cruise observations (Figs. 1-3) suggests that infection prevalence may be elevated very close to shore where *G. delicatula* abundances tend to be especially high. Studies have shown that infection in some freshwater diatom-parasite systems is host density dependent with "epidemics" only observed at relatively high host densities (23), which may explain the differences in infection prevalence between the near-shore MVCO and the broader NES.

A second prominent gradient in *G. delicatula* abundances and infection revealed here is the annual cycle (Figs. 1-3). The largest bloom events typically occurred during or immediately following periods with water temperatures colder than 4 °C while parasitoid infection was negligible (Figs. 1, 4-5), suggesting that temperature may indirectly control *G. delicatula* abundance through its impacts on infection (12). Observations at MVCO further suggest that *G. delicatula* infection remains rare for 60+ days following the cessation of cold temperatures (Figs. 1, 3, 5). Elevated *G. delicatula* infection prevalence during the fall and winter followed by minimal infection in the spring across much of the Mid-Atlantic Bight and Georges Bank (Fig. 2) suggests this pattern holds across much of the NES. Further, from July to September *G. delicatula* was highly abundant while infection was negligible in the northern-most portion of the domain (Fig. 2) where climatological mean SST remains below 4 °C until May (24). Interestingly, the few published observations of *G. delicatula* infection by *C. aestivalis* in other systems (the North and Wadden Seas) were also made during the late summer and fall (7, 11). Together these observations suggest that the annual cycle in *G. delicatula* abundance and infection prevalence may vary spatially across the NES, with northern, colder areas providing longer *G. delicatula* "accumulation windows" by suppressing parasitoid infection. Regression tree analysis suggested that infection in this system may also be suppressed at temperatures >18 °C, but the relatively few observations of elevated *G. delicatula* abundance at these temperatures limits interpretation of this upper bound in the thermal range of infection.

Elucidating the biological mechanisms driving the response of *G. delicatula* infection to temperature will require experimental verification, but our results aid in the development of hypotheses to explain this phenomenon. Some of the five *C. aestivalis* ASVs detected in amplicon sequencing observations at MVCO were present throughout the year, including when temperatures were <4 °C and in the spring and summer following these periods (Figs. 1D, 5C). The presence of some *C. aestivalis* strains during prolonged periods of negligible *G. delicatula* infection shows that some representatives of the *C. aestivalis* species complex likely survive at temperatures <4 °C. Interestingly, the most abundant *C. aestivalis* ASV was not detected during or within 70 days following cold periods, suggesting that microdiversity within the *C. aestivalis* species complex may drive extreme host specificity where only some strains (apparently one at MVCO) infect *G. delicatula*. Differences in host and parasite thermal tolerances have been shown to drive similar responses of diatom abundance and infection to temperature in freshwater diatom-parasite systems (23, 25). We thus hypothesize that temperature-driven local extinction events of a single strain of *C. aestivalis* explains the suppression of *G. delicatula* infection during cold snaps, and that infection is only restored after physical processes "re-seed" this strain of *C. aestivalis*. Unfortunately, the limited accuracy of DADA2 in inferring ASVs from non-overlapping paired reads (26) prohibits definitive statements regarding the importance of *C. aestivalis* microdiversity relative to other potential explanations, such as life cycle transitions or physiological adjustments of *C. aestivalis* to cold temperatures, in explaining the *G. delicatula* infection dynamics observed here.

Our results have important implications for understanding future variability in the NES ecosystem as it is one of the fastest-warming marine ecosystems on Earth (18, 27, 28). The long-term decline in the duration and areal extent of waters with temperatures <4 °C and our observations

of *G. delicatula* abundance and infection (Figs. 4-6) suggest that dramatic changes in the magnitude and phenology of *G. delicatula* accumulation may already be underway on the NES. If these long-term trends continue, impacts might include reduced or a varied composition of phytoplankton biomass available for consumption by larger micro- and mesozooplankton (which may have cascading impacts on the NES food web; (29)) and/or decreased export of diatom biomass and aggregates from the surface ocean to depth (30, 31). These implications point toward an urgent need to develop a predictive understanding of the forcings and impacts of diatom parasitism in economically important coastal ocean ecosystems subject to increasing anthropogenic influence like the NES.

Potential and limitations of automated imaging and classification to quantify phytoplankton parasitism

Microbial interactions shape planktonic food webs and elemental cycles throughout the worlds' oceans (32, 33), but to date these interactions have been difficult to quantify across large spatiotemporal scales due to technical limitations. Parasitism is an understudied planktonic interaction given the proliferation of evidence suggesting that parasites are highly abundant members of marine plankton communities (9, 10). Since diatoms exert disproportionate influence on marine ecosystems, foundational knowledge of the spatiotemporal dynamics and ecology of diatom-parasite interactions is needed to better understand and predict the flow(s) of organic matter through marine food webs (8). This study demonstrates how high-throughput, automated image analysis can be used to quantify diatom parasitism. Here, we discuss the potential and limitations of this approach to advance our understanding of diatom-parasite interactions in the marine environment, and of phytoplankton-parasite interactions in aquatic systems more broadly.

Currently, plankton imaging provides sufficient resolution to identify many microplankton genera and some species. Limited image resolution in combination with low morphological diversity in smaller sized plankton largely precludes taxonomic identification and will likely prevent image-based observation of both free-living parasites and smaller hosts for some time. Our identification of the parasitoid of *G. delicatula* as *C. aestivalis*, and of infected *G. delicatula* images, relied on close agreement of the imaged infection cycle stages with previous, detailed observations of the *C. aestivalis* infection cycle in culture (11, 12). Some uncertainty remains as to whether all infection events identified here were carried out by *C. aestivalis* or another parasitoid with morphologically similar infection dynamics. These caveats demonstrate important considerations for identifying and quantifying parasitic infection in other diatoms and microplankton with automated imaging. Morphological features of infection must be known and resolvable in plankton images to identify infected hosts. These morphological characteristics can be leveraged in cases where the parasitoid is not directly observed, as in morphological responses of *Alexandrium fundyense* to *Ameobophyra sp.* infections (34). In cases where infection cycles or host morphological responses to infection are unknown, recent work (32) suggests that supplementing images with meta-genetic, genomic, or transcriptomic observations to support identification of likely interactions of known or suspected parasites with new hosts may allow for application of these approaches to currently undocumented microplankton-parasite interactions.

Our results highlight several areas where technical advances in plankton imaging and image analysis will facilitate efforts to improve quantitation of diatom and microplankton parasitism. First, reducing uncertainties in estimates of host abundance and infection is possible through continued development of both the instrumentation and machine learning approaches employed here. Higher throughput plankton imaging (35) will reduce sampling uncertainty. Similarly, improvements in automated image classifiers will reduce classification uncertainty. Both improvements will reduce the degree of sample aggregation needed to resolve spatiotemporal gradients and increase resolution of small-scale infection dynamics. Further, improved image classifiers may allow for resolution of additional stages of infection: preliminary classifiers tested in the present study were unable to consistently distinguish *G. delicatula* chains with attached

external nanoflagellates (potentially parasitoids) from other *G. delicatula* morphologies. The automated classifier employed here also required an extensive collection of human-annotated images to ensure consistency and accuracy in both infected and non-infected *G. delicatula* classifications across the billions of images analyzed here. Improvements in machine learning classification may also reduce the required number of human annotations to carry out large-scale investigations of population dynamics. While our optimized "classify and count" approach was highly effective for the applications used here, other studies suggest automated quantifiers may improve estimates of plankton abundance from image data (36, 37). These methods should be more rigorously evaluated for quantification of diatom-parasite interactions. Finally, well-validated segmentation algorithms to quantify both infected and non-infected diatom cell abundances from IFCB or other image data (38) are not currently available, and our study thus focuses on the combined chain and cell abundance and infection prevalence of *G. delicatula*. These and other technical developments will improve resolution of the dynamics and unlock powerful studies of the ecology of microplankton- and diatom-parasite interactions.

Materials and Methods

Imaging-in-flow cytometry

IFCB has been deployed in situ at ~4 m depth at the MVCO offshore tower located in ~15 m water depth off the southern coast of Martha's Vineyard, MA, USA since 2006 (12, 39). IFCB collects discrete seawater samples every ~25 minutes and images particles larger than ~6 µm. Manually classified IFCB images are available from regular biweekly monitoring of IFCB data as well as a previous study that identified *G. delicatula* parasitism in IFCB images from MVCO (12). IFCB has also sampled quasi-continuously from the underway flow-through system on 24 (23 of which are considered here; see Supporting Text), approximately quarterly cruises (conducted by the NOAA EcoMon program, e.g. (40)) that surveyed the NES since 2013. Winter is under-sampled with only one cruise available, but all other seasons included seven or more cruises. Additional details are provided in Supporting Text.

Amplicon sequencing

Amplicon sequencing observations from MVCO are considered to determine the presence or absence of *C. aestivalis* in the water column independently from observations of *G. delicatula* infection (free-living *C. aestivalis* cannot be unambiguously identified in IFCB images). A total of 135 samples were collected for amplicon sequencing of the V4 hypervariable region of the 18S rRNA gene from February 2013 to December 2021. 18S rRNA gene amplicons were generated with the 574*f and 1132r primers from (41) (CGGTAAYTCCAGCTCYV; CCGTCAATTHCTTYAART) and sequenced on an Illumina MiSeq (see Supporting Text for complete methods). Demultiplexed sequence data were processed using the DADA2 method (26) with some modifications to accommodate non-overlapping paired reads (Supporting Text). BLAST analysis (42) showed that 5 ASVs were perfect matches to at least one *C. aestivalis* reference sequence included in the Protistan Ribosomal Reference database v4.14.0 (43); these ASVs are considered here.

In situ and remotely sensed temperature observations

Water temperature observations at MVCO are derived from a SeaBird Electronics MicroCAT CTD deployed alongside the IFCB at the offshore tower. Where water temperature observations are not available, observations from another MicroCAT CTD deployed at ~12 m depth at an undersea node ~1.5 km from the IFCB deployment site are used to fill gaps in the offshore tower's temperature time series. Across the broader NES, a combination of underway water temperature and satellite-measured sea surface temperature (SST) observations are considered. Underway

observations are considered for estimates of water temperature concurrent with IFCB observations (Fig. 4), while satellite SST is used in composite maps (Figs. 1-2) and long-term trend analyses (Fig. 6). Supporting Text provides detailed analysis methods for these data.

Automated image classification

A convolutional neural network (CNN) image classifier with Inception v3 architecture (13) was used for automated classification of IFCB images. A training set of at least 20 and at most 2000 manually annotated images from each of 155 classes was used for training and initial validation of the classifier. The classifier was initialized with pre-trained weights from ImageNet (44) and fine-tuned with the NES IFCB training set (97026 images, 155 classes, 80-20 split for training and validation). The classifier performed well in initial validations based on the 20% hold-out set with an F1 statistic (harmonic mean of precision and recall) across all classes of 0.91.

Two classes of *G. delicatula* were separated by the CNN classifier: *G. delicatula* and infected *G. delicatula* (Fig. S1). The "*G. delicatula*" class includes images of *G. delicatula* cells and chains exhibiting a range of morphological features, as well as some images depicting *G. delicatula* cells or chains with small flagellates (potentially parasitoids) apparently attached to the exterior of the frustule (Fig. S1). *G. delicatula* images with externally-attached nanoflagellates were included in the non-infected *G. delicatula* class rather than the infected *G. delicatula* class for two reasons: host responses to external parasitoid attachment are unknown and could include successful defense against infection, and other nanoflagellates may interact with *G. delicatula*. The class "infected *G. delicatula*" includes images of *G. delicatula* cells or frustules that exhibit signs of current or recent parasitoid presence within the host frustule (Fig. S1). The class-specific F1 statistics for automated classifications of *G. delicatula* and infected *G. delicatula* images using the "hold-out" subset of the classifier training set were 0.92 and 0.91, respectively.

Manually annotated images from MVCO independent from those considered in classifier training were used to optimize and evaluate classifier performance when applied to novel IFCB observations. Classifier optimization is described in Supporting Text and sought to equate precision and recall statistics (and thus, false positive and negative classification errors) for *G. delicatula* and infected *G. delicatula* classifications. The F1 statistics obtained for *G. delicatula* and infected *G. delicatula* in the MVCO validation set after optimization were 0.92 and 0.78, respectively. Estimates of *G. delicatula* and infected *G. delicatula* abundances and *G. delicatula* infection prevalence based on human and automated classifiers were in close agreement with one another (Supporting Text; Fig. S2-S3).

The same optimized classifier was applied and additional classifier validation was performed for shipboard IFCB observations (Supporting Text). In these data, automated *G. delicatula* classifications achieved an F1 value of 0.91 with precision and recall values of 0.92 and 0.90, while infected *G. delicatula* classifications had an F1 value of 0.50 and precision and recall values of 0.52 and 0.48. Following image classification, counts of *G. delicatula* and infected *G. delicatula* chains (it is currently not possible to enumerate individual cells in IFCB images of diatoms) were determined for discrete IFCB samples.

Spatiotemporal distributions and gradients

Maps were created with the m_map MATLAB toolbox (45). We used a spatial sample aggregation procedure to reduce uncertainty in *G. delicatula* abundance and infection estimates and smooth the data for inspection of large-scale spatial distributions (Supporting Text, Fig. S4-S5). Monthly aggregate abundances and infection prevalence were used to quantify seasonal gradients. To characterize cross-shore gradients the Climate Data Toolbox (46) was used to compute great circle distances from each IFCB sample to the nearest coastline. We characterize gradients across the four major "Ecological Production Units" on the NES (16, 17) after slightly

modifying the boundaries used by (17) to incorporate more of the available IFCB data (Fig. S6). Spatiotemporal gradients across each of these dimensions are characterized by aggregating discrete IFCB samples and estimating uncertainty as described in Supporting Text.

Regression tree analysis

A bootstrap-aggregated ensemble of 100 regression trees was fit to both the shipboard and daily-aggregated MVCO data sets of concurrent *G. delicatula* infection prevalence and temperature observations. Our goal in this analysis was to objectively determine critical temperature thresholds that may result in dramatic changes in *G. delicatula*'s susceptibility to infection. For this reason, each regression tree was constrained to include only 2 splits. Concurrent temperature and infection prevalence values were only included in this analysis where *G. delicatula* abundances were >5 chains ml^{-1} to prevent biasing results toward highly uncertain infection prevalence estimates. The partial dependences of infection prevalence on temperature in each data set illustrate predicted values of infection prevalence from a given temperature value from the ensemble tree.

Acknowledgments

We acknowledge the captains and crews of the vessels used to collect the data presented here, NOAA's support of the survey cruises considered here, and the MVCO Operations Team for maintaining the facility. We are grateful to R. Olson and A. Shalapyonok for their dedicated contributions to maintaining the IFCB time series at MVCO. We also thank two anonymous peer reviewers and the editorial team at PNAS for their contructive and timely review of our manuscript. Amplicon sequencing was accomplished with the use of sequencing services at the Rhode Island Institutional Development Award (IDeA) Network of Biomedical Research Excellence from the National Institute of General Medical Sciences of the National Institutes of Health under grant number P20GM103430 through the Centralized Research Core facility and/or the Molecular Informatics Core (RRID:SCR_017685). Financial support for this work was provided by the Simons Foundation (561126); the National Science Foundation (OCE-1434440; OCE-1851012), especially through the Northeast U.S. Shelf Long Term Ecological Research (OCE-1655686); fellowship support (to HMS) through the NOAA Cooperative Institute for the North Atlantic Region (CINAR) under Cooperative Agreement NA14OAR4320158; and fellowship support (to DC) by the National Science Foundation (OCE-2205596).

References

1. J. H. Ryther, Photosynthesis and Fish Production in the Sea. *Science* **166**, 72–76 (1969).

2. P. Tréguer, *et al.*, Influence of diatom diversity on the ocean biological carbon pump. *Nature Geosci* **11**, 27–37 (2018).

3. R. T. Barber, M. R. Hiscock, A rising tide lifts all phytoplankton: Growth response of other phytoplankton taxa in diatom-dominated blooms. *Global Biogeochemical Cycles* **20** (2006).

4. V. Smetacek, Diatoms and the Ocean Carbon Cycle. *Protist* **150**, 25–32 (1999).

5. E. B. Sherr, B. F. Sherr, Heterotrophic dinoflagellates: a significant component of microzooplankton biomass and major grazers of diatoms in the sea. *Marine Ecology Progress Series* **352**, 187–197 (2007).

6. L. P. M. J. Wetsteyn, L. Peperzak, Field observations in the Oosterschelde (The Netherlands) on Coscinodiscus concinnus and Coscinodiscus granii (Bacillariophyceae)

infected by the marine fungus Lagenisma coscinodisci (Oomycetes). *Hydrobiological Bulletin* **25**, 15–21 (1991).

7. U. Tillmann, K.-J. Hesse, A. Tillmann, Large-scale parasitic infection of diatoms in the Northfrisian Wadden Sea. *Journal of Sea Research* **42**, 255–261 (1999).

8. B. Scholz, *et al.*, Zoosporic parasites infecting marine diatoms – A black box that needs to be opened. *Fungal Ecology* **19**, 59–76 (2016).

9. G. Lima-Mendez, *et al.*, Determinants of community structure in the global plankton interactome. *Science* **348**, 1262073 (2015).

10. F. Vincent, C. Bowler, Diatoms Are Selective Segregators in Global Ocean Planktonic Communities. *mSystems* **5**, e00444-19 (2020).

11. G. Drebes, S. F. Kühn, A. Gmelch, E. Schnepf, Cryothecomonas aestivalis sp. nov., a colourless nanoflagellate feeding on the marine centric diatom Guinardia delicatula (Cleve) Hasle. *Helgolander Meeresunters* **50**, 497–515 (1996).

12. E. E. Peacock, R. J. Olson, H. M. Sosik, Parasitic infection of the diatom *Guinardia delicatula*, a recurrent and ecologically important phenomenon on the New England Shelf. *Marine Ecology Progress Series* **503**, 1–10 (2014).

13. C. Szegedy, *et al.*, Going deeper with convolutions in *2015 IEEE Conference on Computer Vision and Pattern Recognition (CVPR)*, (IEEE, 2015), pp. 1–9.

14. D. W. Henrichs, S. Anglès, C. C. Gaonkar, L. Campbell, Application of a convolutional neural network to improve automated early warning of harmful algal blooms. *Environ Sci Pollut Res* **28**, 28544–28555 (2021).

15. R. Fuchs, *et al.*, Automatic recognition of flow cytometric phytoplankton functional groups using convolutional neural networks. *Limnology and Oceanography: Methods* **20**, 387–399 (2022).

16. S. M. Lucey, M. J. Fogarty, Operational fisheries in New England: Linking current fishing patterns to proposed ecological production units. *Fisheries Research* **141**, 3–12 (2013).

17. J. J. Suca, *et al.*, Sensitivity of sand lance to shifting prey and hydrography indicates forthcoming change to the northeast US shelf forage fish complex. *ICES Journal of Marine Science*, fsaa251 (2021).

18. Z. Chen, *et al.*, Long-Term SST Variability on the Northwest Atlantic Continental Shelf and Slope. *Geophysical Research Letters* **47**, e2019GL085455 (2020).

19. J. A. Yoder, S. E. Schollaert, J. E. O'Reilly, Climatological phytoplankton chlorophyll and sea surface temperature patterns in continental shelf and slope waters off the northeast U.S. coast. *Limnology and Oceanography* **47**, 672–682 (2002).

20. C. B. Mouw, J. A. Yoder, Primary production calculations in the Mid-Atlantic Bight, including effects of phytoplankton community size structure. *Limnology and Oceanography* **50**, 1232–1243 (2005).

21. X. Pan, A. Mannino, H. G. Marshall, K. C. Filippino, M. R. Mulholland, Remote sensing of phytoplankton community composition along the northeast coast of the United States. *Remote Sensing of Environment* **115**, 3731–3747 (2011).

22. Z. Zang, *et al.*, Spatially varying phytoplankton seasonality on the Northwest Atlantic Shelf: a model-based assessment of patterns, drivers, and implications. *ICES Journal of Marine Science* (2021) https:/doi.org/10.1093/icesjms/fsab102 (June 15, 2021).

23. B. W. Ibelings, *et al.*, Chytrid infections and diatom spring blooms: paradoxical effects of climate warming on fungal epidemics in lakes. *Freshwater Biology* **56**, 754–766 (2011).

24. A. C. Thomas, *et al.*, Seasonal trends and phenology shifts in sea surface temperature on the North American northeastern continental shelf. *Elementa: Science of the Anthropocene* **5**, 48 (2017).

25. A. S. Gsell, L. N. de S. Domis, E. van Donk, B. W. Ibelings, Temperature Alters Host Genotype-Specific Susceptibility to Chytrid Infection. *PLOS ONE* **8**, e71737 (2013).

26. B. J. Callahan, *et al.*, DADA2: High-resolution sample inference from Illumina amplicon data. *Nat Methods* **13**, 581–583 (2016).

27. R. K. Shearman, S. J. Lentz, Long-term sea surface temperature variability along the U.S. east coast. *J. Phys. Oceanogr.* **40**, 1004–1017 (2010).

28. M. T. Burrows, *et al.*, The Pace of Shifting Climate in Marine and Terrestrial Ecosystems. *Science* **334**, 652–655 (2011).

29. P. G. Verity, V. Smetacek, Organism life cycles, predation, and the structure of marine pelagic ecosystems. *Marine Ecology Progress Series* **130**, 277–293 (1996).

30. J. T. Allen, *et al.*, Diatom carbon export enhanced by silicate upwelling in the northeast Atlantic. *Nature* **437**, 728–732 (2005).

31. A. E. S. Kemp, J. Pike, R. B. Pearce, C. B. Lange, The “Fall dump” — a new perspective on the role of a “shade flora” in the annual cycle of diatom production and export flux. *Deep Sea Research Part II: Topical Studies in Oceanography* **47**, 2129–2154 (2000).

32. A. Z. Worden, *et al.*, Rethinking the marine carbon cycle: Factoring in the multifarious lifestyles of microbes. *Science* **347**, 1257594 (2015).

33. J. J. Pierella Karlusich, *et al.*, Global distribution patterns of marine nitrogen-fixers by imaging and molecular methods. *Nat Commun* **12**, 4160 (2021).

34. M. L. Brosnahan, *et al.*, Rapid growth and concerted sexual transitions by a bloom of the harmful dinoflagellate Alexandrium fundyense (Dinophyceae). *Limnology and Oceanography* **60**, 2059–2078.

35. R. J. Olson, A. Shalapyonok, D. J. Kalb, S. W. Graves, H. M. Sosik, Imaging FlowCytobot modified for high throughput by in-line acoustic focusing of sample particles. *Limnology and Oceanography: Methods* **15**, 867–874 (2017).

36. E. C. Orenstein, *et al.*, Semi- and fully supervised quantification techniques to improve population estimates from machine classifiers. *Limnology and Oceanography: Methods* **18**, 739–753 (2020).

37. P. González, *et al.*, Automatic plankton quantification using deep features. *Journal of Plankton Research* **41**, 449–463 (2019).

38. E. C. Orenstein, *et al.*, Machine learning techniques to characterize functional traits of plankton from image data. *Limnology and Oceanography* **67** (2022).

39. R. J. Olson, H. M. Sosik, A submersible imaging-in-flow instrument to analyze nano-and microplankton: Imaging FlowCytobot. *Limnology and Oceanography: Methods* **5**, 195–203 (2007).

40. J. Prezioso, Cruise Results GU 21-02 Spring Ecosystem Monitoring Cruise Report (2022) https:/doi.org/10.25923/4W08-1D30 (February 14, 2023).

41. L. W. Hugerth, *et al.*, Systematic Design of 18S rRNA Gene Primers for Determining Eukaryotic Diversity in Microbial Consortia. *PLOS ONE* **9**, e95567 (2014).

42. S. F. Altschul, W. Gish, W. Miller, E. W. Myers, D. J. Lipman, Basic local alignment search tool. *Journal of Molecular Biology* **215**, 403–410 (1990).

43. L. Guillou, *et al.*, The Protist Ribosomal Reference database (PR2): a catalog of unicellular eukaryote Small Sub-Unit rRNA sequences with curated taxonomy. *Nucleic Acids Research* **41**, D597–D604 (2013).

44. O. Russakovsky, *et al.*, ImageNet Large Scale Visual Recognition Challenge. *Int J Comput Vis* **115**, 211–252 (2015).

45. Pawlowicz, R., 2020., M_Map: A mapping package for MATLAB.

46. C. A. Greene, *et al.*, The Climate Data Toolbox for MATLAB. *Geochemistry, Geophysics, Geosystems* **20**, 3774–3781 (2019).

Figures Captions

Figure 1. Spatiotemporal dynamics of *G. delicatula* abundance and parasitoid infection. Maps show composites of (A) total *G. delicatula* abundance and (B) infection prevalence and (C) mean satellite sea surface temperature during the period over which these cruises took place. The color bar in (A) is truncated at 20 chains ml^{-1}. Black lines in (C) show the boundaries of "Ecological Production Units" previously defined for the Northeast U.S. Shelf (17). Infection prevalence is not shown where host abundance is <1 chain ml^{-1} due to high uncertainty. Time series observations are daily (D) aggregate *G. delicatula* abundance (dots) and infection prevalence (dot color) and (E) mean in-situ water temperature at MVCO. The y-axis and colorbar in (D) are truncated at 200 chains ml^{-1} and 20%, respectively. Pink triangles in (D) from 2013-2021 indicate where at least one *C. aestivalis* ASV was (filled) or was not (open) detected in amplicon sequencing observations. Gray shading indicates periods where water temperature was <4 °C.

664 **Figure 2.** Composite maps of (A, D, G, J) total *G. delicatula* abundance and (B, E, H, K) infection
665 prevalence and (C, F, I, L) mean satellite sea surface temperature during each season from
666 2013-2021. Infection prevalence is not shown where host abundance is <1 chain ml^{-1} due to high
667 uncertainty. Abundance colorbars are truncated at 20 chains ml^{-1}, infection prevalence colorbars
668 are truncated at 10%, and temperature colorbars are truncated at 4 °C.
669
670

Figure 3. Spatiotemporal gradients in *G. delicatula* abundance (navy) and infection prevalence (pink). Shown are (A, B) monthly aggregate abundance and infection prevalence (A) at the nearshore Martha's Vineyard Coastal Observatory (MVCO) time series and (B) across the broader Northeast U.S. Shelf, and (C) cross-shore and (D) inter-region gradients. (B-D) do not consider observations at MVCO. Error bars show 95% confidence intervals for aggregate concentrations assuming counts are drawn from a Poisson distribution. Note that scales vary across different panels.

Figure 4. Role of temperature in governing *G. delicatula* parasitoid infection dynamics (A) at MVCO and (B) across the broader NES. (C) shows the partial dependence of infection prevalence on temperature determined from regression tree analysis (left axis) and the number of observations in each temperature bin (right axis) at MVCO (black) and across the broader NES (red). In all panels, vertical dashed lines indicate 4 °C and observations are only considered where *G. delicatula* abundance is >5 chains ml^{-1}. Observations at MVCO are daily aggregate quantities. The colorbar is truncated at 50 chains ml^{-1} to facilitate visualization of abundances.

689 **Figure 5.** Continued suppression of infection following cold periods. (A) shows the number of
690 days with aggregate *G. delicatula* abundance >5 chains ml^{-1} (navy) coincident with infection
691 prevalence >5% (pink) relative to the number of days since daily average temperatures were <4
692 °C across all years at Martha's Vineyard Coastal Observatory (MVCO). (B) shows these data for
693 individual years with black numbers showing the number of days with aggregate *G. delicatula*
694 abundance >5 chains ml^{-1} and tile color indicating the fraction of those days with infection
695 prevalence >5%. (C) shows relative frequencies of detection of the five *C. aestivalis* ASVs
696 detected in amplicon sequencing observations relative to the number of days to detection of each
697 ASV following an observation of water temperature <4 °C across all years at MVCO. *C. aestivalis*
698 ASVs are numbered according to their rank order cumulative relative abundance across all
699 available samples, with ASV1 the most abundant.

700

701 **Figure 6.** Long-term trend in the spatiotemporal extent of cold periods on the Northeast U.S.
702 Shelf (NES). Shown are (A) a daily time series of the areal extent of waters with sea surface
703 temperature (SST) <4 °C on the NES and (B) its annual integral. The red line in (B) indicates the
704 long-term linear trend determined by linear regression.
705

706

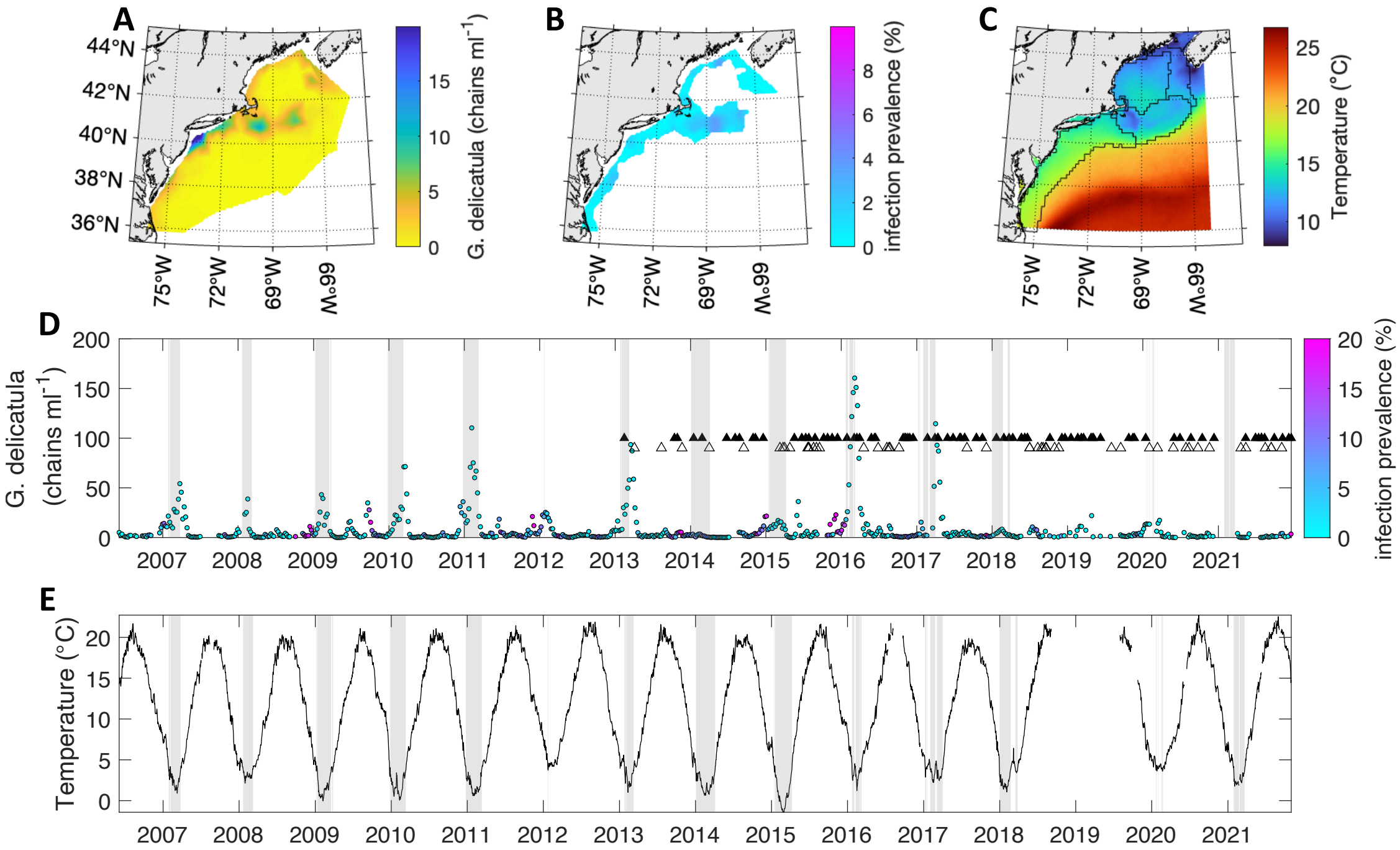
A
44°N
42°N
40°N
38°N
36°N
75°W
72°W
69°W
M◦99
15
10
5
0
G. delicatula (chains ml^{-1})
B
8
6
4
2
0
infection prevalence (%)
C
25
20
15
10
Temperature (°C)
D
G. delicatula (chains ml^{-1})
200
150
100
50
0
2007
2008
2009
2010
2011
2012
2013
2014
2015
2016
2017
2018
2019
2020
2021
20
15
10
5
0
infection prevalence (%)
E
Temperature (°C)
20
15
10
5
0

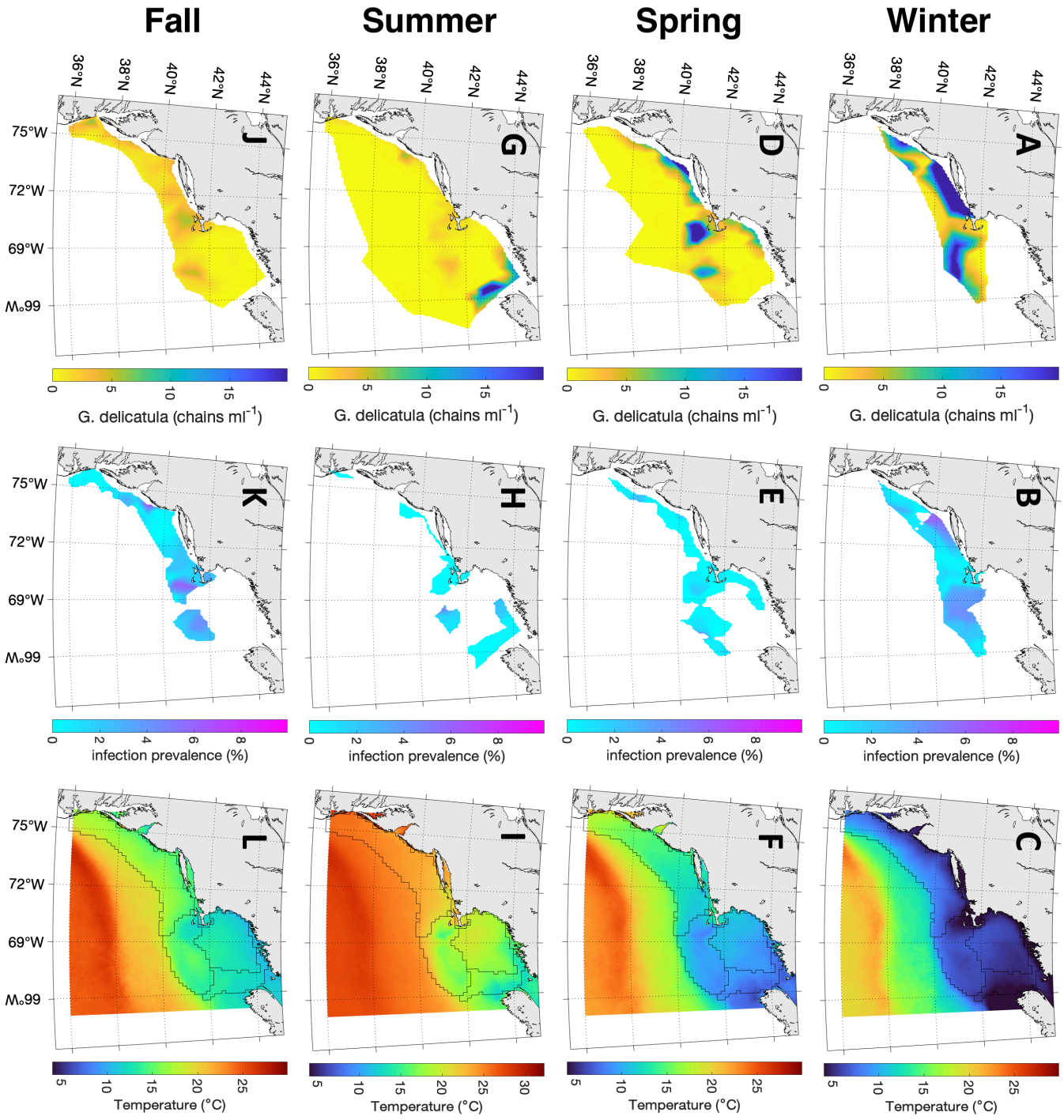
Fall
Summer
Spring
Winter
36°N
38°N
40°N
42°N
44°N
75°W
72°W
69°W
M₀99
J
G
D
A
K
H
E
B
L
I
F
C
0
5
10
15
G. delicatula (chains ml^{-1})
0
2
4
6
8
infection prevalence (%)
5
10
15
20
25
30
Temperature (°C)

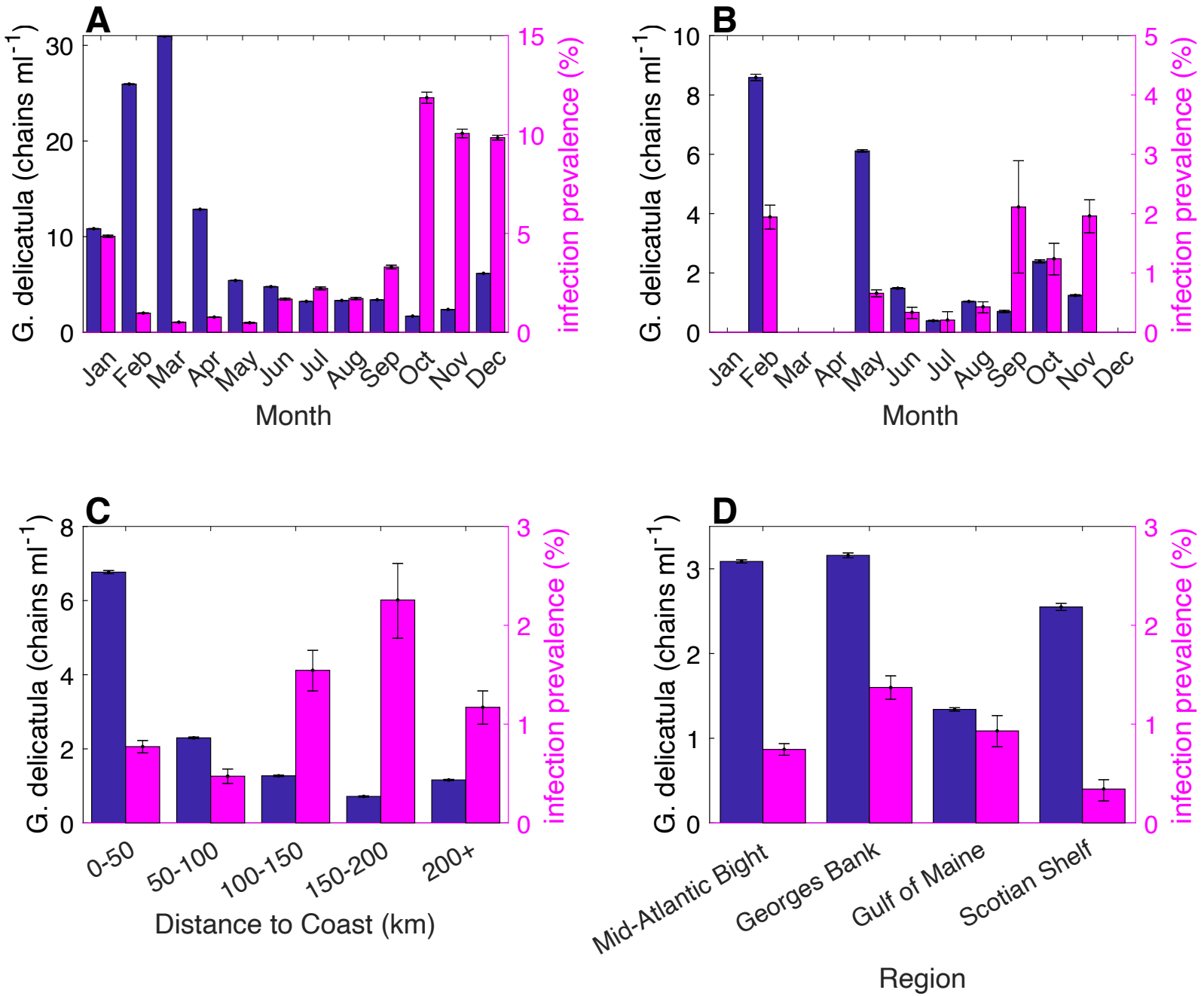
A
G. delicatula (chains ml-1)
infection prevalence (%)
Jan
Feb
Mar
Apr
May
Jun
Jul
Aug
Sep
Oct
Nov
Dec
Month
B
G. delicatula (chains ml-1)
infection prevalence (%)
Month
C
G. delicatula (chains ml-1)
infection prevalence (%)
0-50
50-100
100-150
150-200
200+
Distance to Coast (km)
D
G. delicatula (chains ml-1)
infection prevalence (%)
Mid-Atlantic Bight
Georges Bank
Gulf of Maine
Scotian Shelf
Region

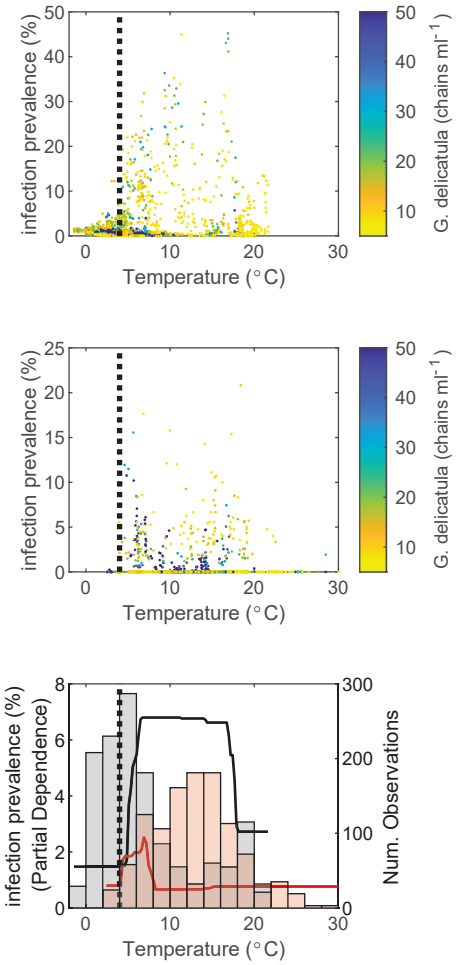
infection prevalence (%)
Temperature (°C)
G. delicatula (chains ml^{-1})
infection prevalence (%)
Temperature (°C)
G. delicatula (chains ml^{-1})
infection prevalence (%)
(Partial Dependence)
Num. Observations
Temperature (°C)

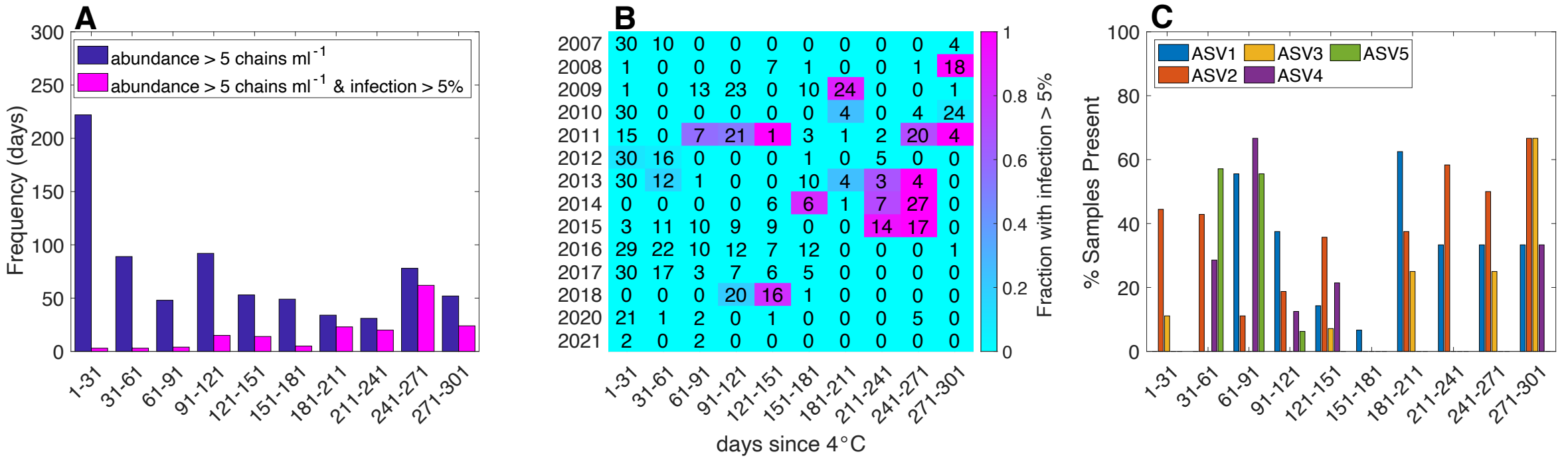
A
abundance > 5 chains ml-1
abundance > 5 chains ml-1 & infection > 5%
Frequency (days)
0
50
100
150
200
250
300
1-31
31-61
61-91
91-121
121-151
151-181
181-211
211-241
241-271
271-301
B
2007 30 10 0 0 0 0 0 0 0 4
2008 1 0 0 0 7 1 0 0 1 18
2009 1 0 13 23 0 10 24 0 0 1
2010 30 0 0 0 0 0 4 0 4 24
2011 15 0 7 21 1 3 1 2 20 4
2012 30 16 0 0 0 1 0 5 0 0
2013 30 12 1 0 0 10 4 3 4 0
2014 0 0 0 0 6 6 1 7 27 0
2015 3 11 10 9 9 0 0 14 17 0
2016 29 22 10 12 7 12 0 0 0 1
2017 30 17 3 7 6 5 0 0 0 0
2018 0 0 0 20 16 1 0 0 0 0
2020 21 1 2 0 1 0 0 0 5 0
2021 2 0 2 0 0 0 0 0 0 0
1-31
31-61
61-91
91-121
121-151
151-181
181-211
211-241
241-271
271-301
days since 4°C
Fraction with infection > 5%
0
0.2
0.4
0.6
0.8
1
C
ASV1
ASV2
ASV3
ASV4
ASV5
% Samples Present
0
20
40
60
80
100
1-31
31-61
61-91
91-121
121-151
151-181
181-211
211-241
241-271
271-301

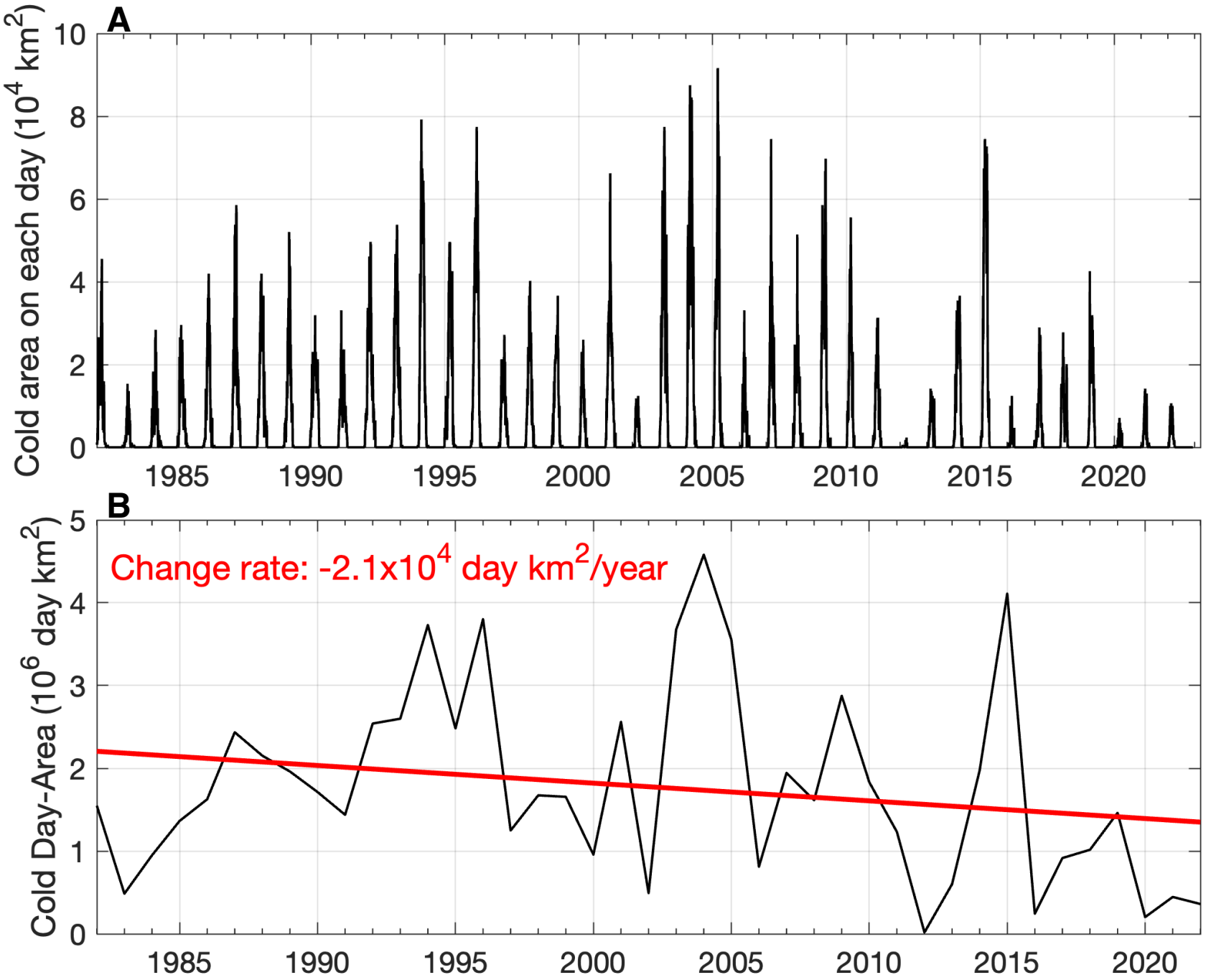
A
Cold area on each day (10^4 km^2)
0
2
4
6
8
10
1985
1990
1995
2000
2005
2010
2015
2020
B
Cold Day-Area (10^6 day km^2)
Change rate: -2.1x10^4 day km^2/year
0
1
2
3
4
5
1985
1990
1995
2000
2005
2010
2015
2020